scientific reports

Check for updates

OPEN

Implementation of a hybrid neural network control technique to a cascaded MLI based SAPF

Rashmi Rekha Behera[1], Ashish Ranjan Dash[1], Satyasis Mishra[1], Anup Kumar Panda[2] & Demissie Jobir Gelmecha[3]✉

This paper presents a naïve back propagation (NBP) based $i \cos \emptyset$ technique implemented to a cascaded multilevel inverter (MLI) based shunt active power filter (SAPF). The recommended control algorithm is applied to extract the fundamental component of load current and to decide the compensating current reference for harmonic elimination. The performance of the SAPF using the proposed NBP-based $i \cos \emptyset$ technique is compared with another two classical control techniques, such as, $i_d - i_q$ technique and $i \cos \emptyset$ technique. The accuracy of the proposed control technique depends on the tuned estimation of active and reactive weights. The performance study of the proposed SAPF with the proposed control technique is investigated under non-linear conditions, with balanced and unbalanced loading conditions. The results reveal that the recommended SAPF is efficient enough to reduce the harmonics from the source current with smooth variation in DC link voltage. The effectiveness of the proposed method is validated by simulation using MATLAB Simulink, and the real-time results are also validated by the experimental setup.

With a fabulous expansion in extremely nonlinear load implementations, the power grid system agonizes from various complications in power condition and quality. Expansion in renewable or inexhaustible energy resource applications also influences the quality of power. Generally, the power quality is mainly concerned with the condition of voltage and current. The voltage characteristic of the system entirely depends on the grid or supply voltage. Similarly, the current characteristic of the system entirely relies upon the load current. The low power quality consists of issues like voltage disparity in phases, harmonics in wave shape of voltage and current, swelling voltage, sagging voltage and flickering in voltage, imbalance in reactive power and also power blackout, etc. In the current situation, the active power filter (APF) is the most appropriate technique to deal with the issues regarding the quality of power. The implementation of APFs has been initiated to overcome the issues depicted before regarding the quality of electrical power[1]. There are various active power filters (APF) that are ready in the market for use in the quality improvement of electrical power; those are series APF[2,3], shunt APF[4–6] and unified power quality conditioner (UPQC)[7]. In the class of numerous APFs, shunt APFs are remarkably adequate during highly nonlinear loading conditions[8,9]. The SAPF is an effective device, which can inject current at PCC (point of common coupling) to recompense the harmonics in the supply current to make it sinusoidal.

Generally, the basic building blocks of a shunt APF are inverter (CSI/VSI), dc-link unit, control circuit, and inductive filter (discretionary). Out of the numerous types of SAPF, usually the APFs based on VSIs[7] are more adopted due to reliability in nature. But, for high voltage applications, these classical VSIs are unable to deal with the device stress and losses. On the other hand the MLIs[10,11] are capable to deal with high voltage applications with comparatively low switching frequency. Its harmonic minimization ability is also higher than traditional VSIs. As the classical MLIs are having a shortcoming of using a huge number of DC-link unit capacitors, which leads to an increase in the intricacy of the control system. Voltage balancing along with power-sharing becomes more problematic. And also, there will be a reduction in reliability as the capacitors count increases. With the increasing use of capacitors, it leads to more failure rate, as the capacitors are very venerable to faults[12]. This complication can be handled by reducing the requirement of capacitances in the DC link by using transformers in a cascaded manner. It can also produce a higher count of voltage steps by increasing the number of modules.

[1]Centurion University of Technology and Management, Paralakhemundi, Odisha, India. [2]National Institute of Technology, Rourkela, Odisha, India. [3]Adama Science and Technology University, Adama, Ethiopia. ✉email: gelmechad@gmail.com

nature portfolio

1

With the application of transformers, the reliability increases due to a reduction in the number of capacitors in the system, and it also reduces the control problems. It contributes to the galvanic isolation of the grid system from the inverter.

This work approaches a novel MLI configuration[13] which is cascaded through coupled transformer operating as a SAPF. This framework is based on traditional three-phase VSIs as the building blocks of the MLI. These voltage source inverter bridges are coupled with transformers, which are cascaded together to feed the grid system. This multilevel inverter can attain multiple levels of voltage steps with a minimum number of semiconductor switches as compared to other conventional MLIs. This multilevel voltage waveform can be achieved by implementing an appropriate modulation method and also appropriate turn ratios of the cascaded transformers.

The control system of a SAPF is very important for the effective operation of the SAPF connected to the grid system. Various control techniques and their applications are focused on the research area of SAPF. Few of them are p-q technique[14], $(i_d - i_q)$ method[15], non-linear control methods, Lyapunov function-based method[16], $i \cos \emptyset$ control method[17] and many more. In last two decades, the artificial neural network (ANN) has significant progress in the research and application field. In[18] an intelligent ANN-based swift harmonic detection system is described. In[19] Hopfield ANN technique is analyzed for the detection of harmonics. Some more applications of ANN in the monitoring of harmonic distortion are explained in[20,21]. The major issue regarding the utilization of ANNs is picking up accurate dimensions and proper network topology. This turns into more complicated during training to very small error signals[22]. To overcome these complexities various mathematical replica is applied for one-step sizing, weight amendment, and normalization activity. It contributes to better response in an unsteady situation to control the SAPF in varying load conditions. Kernel incremental meta-learning process[23] and ANN-based conductance estimation[24] are implemented for a better solution for power quality issues. In[25,26], EMD-based control strategy shows a real-time approach to reducing source current harmonics.

Out of various ANN techniques, the Naive back propagation (NBP) technique has a higher ability to treat the complex non-linear condition. The major advantages of this technique are self-organizing, adaptive learning, fault tolerance due to redundant information, and real-time implementation. In this work, detailed information of the estimation of the control technique followed by mathematical modeling is presented. The first layer of the ANN network is estimated by using the $i \cos \emptyset$ technique. By applying the sigmoidal criterion, the weighted components of load current for each phase are calculated. The initial weights for both outer and inner layers are applied. The weight correction is done by using the NBP method. Because of this, sizing adjustment, and adaptive learning function for the ANN are not necessary. There are various hybrid ANN techniques available in the literature[27–29,35,36]. Out of these NBP based $i\cos\emptyset$ control method is implemented for our proposed SAPF. This algorithm is very much useful for weighting factor extraction, and weight correction for the variable non-linear load current.

Proposed SAPF configuration

The proposed framework presented in Fig. 1 is consisting of an MLI, based on classical three-phase VSI bridges cascaded through coupled transformers, which feed the compensating current to the grid system. This MLI is coupled with the grid system at the common coupling position (PCC) as a SAPF. This suggested MLI topology can produce a higher count of voltage levels as compared to other classical topologies[30]. In this work a general framework is presented, where K numbers of VSI bridges are used. These bridges are cascaded through coupling transformers. Each VSI bridge with its coupled transformers can be considered as a single module. Each module is consisting of three legs for three different phases. Each leg has two switches (p_{kj} and q_{kj}). The subscript 'k' represents the unit or cell number ($k = 1, 2, 3…K$), and similarly the subscript 'j' represents the phase name (j = a, b, c). So, there are six semiconductor devices in the three legs of each module. In total there are 6 K semiconductor devices in the suggested framework. The two switches in a leg are operated in a complementary state to one another to prevent short circuits of DC-link or uncertain voltage produced by the module. Therefore, exclusively eight possible switching states are possible for a single module. Therefore, the possible voltage levels per phase are $2v_{dc}/3$, $v_{dc}/3$, $-v_{dc}/3$ and $-2v_{dc}/3$ which appear across the primary winding of the transformers, where v_{dc} represents the voltage at the DC link. That is why we can get four voltage levels at the output of a single module.

The v'_{kj} is the secondary voltage of the coupled transformer.

$$v'_{kj} = N_k v_{kj} \tag{1}$$

So, the total resultant phase voltage of the cascaded secondary windings of the transformer per phase is v'_j

$$v'_j = \sum_{k=1}^{K} v'_{kj} \tag{2}$$

Let the smoothing inductance is l_{sh} at the PCC, and the equivalent resistance of SAPF is r_{sh}. Then,

$$v'_j - v_{gs} = \left[l_{sh} \frac{di_{shj}}{dt} + r_{sh}i_{shj} - l_g \frac{di_{gj}}{dt} - r_g i_{gj} + e_{gj} \right] \tag{3}$$

where, v_{gs} is the voltage between the grid to the neutral point of the SAPF. e_{gj} is the grid source voltage that is presented in Fig. 2. At PCC, the current equation applying KCL can be presented as
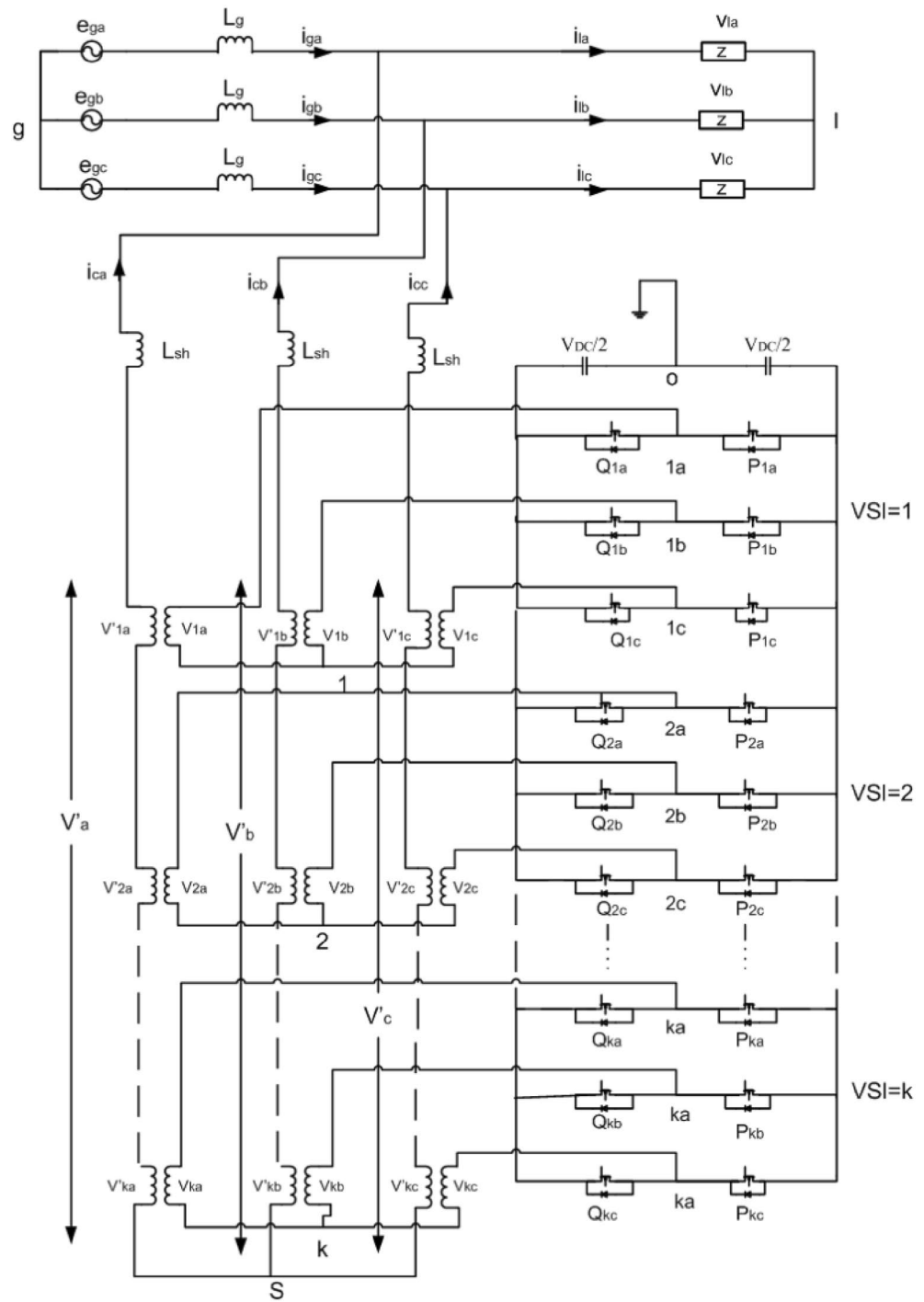
$$i_{shj} = i_{lj} - i_{gj} \tag{4}$$

Figure 1. Suggested cascaded SAPF framework.

Putting the value of i_{shj} from (4) in (3) we get

$$v'_j - v_{gs} = \left[-\left(l_g + l_{sh}\right)\frac{di_{gj}}{dt} - \left(r_g + r_{sh}\right)i_{gj} \right] + \left[l_{sh}\frac{di_{lj}}{dt} + r_{sh}i_{lj} + e_{gj} \right] \tag{5}$$

In (5) the second part of the right-hand side terms is the trepidation, which is to be recompensed by the SAPF (shunt active power filter). The resultant voltage of the transformer at the secondary winding is also denoted as
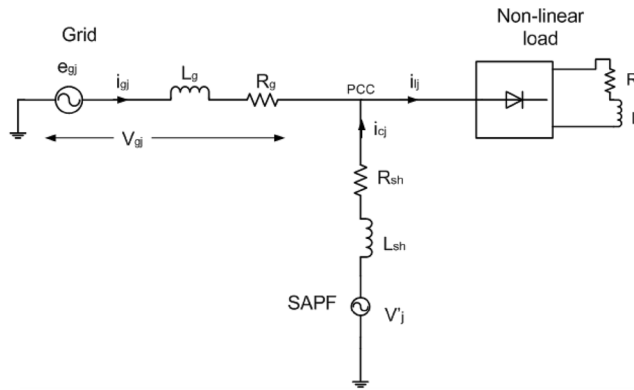
$$v'_j = v'_{j0} - v'_0 \tag{6}$$

Figure 2. Single-line network diagram of the suggested SAPF coupled to grid.

$$v'_{j0} = \sum_{k=1}^{K} N_k v_{kj0} \tag{7}$$

$$v'_0 = \sum_{k=1}^{K} N_k v_{k0} = \sum_{k=1}^{K} \left(\frac{N_k}{3} \sum_j v_{kj0} \right) \tag{8}$$

Now putting the value of v'_0 from (8) into (6) we get

$$v'_j = v'_{j0} - \left[\sum_{k=1}^{K} \left(\frac{N_k}{3} \sum_j v_{kj0} \right) \right] \tag{9}$$

We are able to develop a maximum 4Kcountof voltage levels in v'_j by considering the turns ratio of the transformers to be equal to one (i.e. $N_k = 1$). So, we can achieve a maximum of eight voltage steps in a two-module structure, and in that way, 12 voltage steps can be achieved by the three-module configuration of the MLI. Even, we can bring out a higher number of voltage steps in v'_j by allowing the turn ratios in a proper pattern for the transformers (i.e., $N_k = 2^{k-1}$). Taking the turn ratios in the proposed pattern we can achieve 12 voltage levels per phase in a two-module MLI, and twenty-eight voltage levels in a three-module MLI. We can get up to $2 \times \sum_{k=1}^{M} 2^k$ number of voltage steps by taking the turn ratios for the transformer in the pattern of $N_k = 2^{k-1}$.

Reference compensating current generation
For precise execution of the SAPF, is most important that the reference current has to be generated correctly. The capacitance–voltage of the DC link performs a significant role in finding out the reference current during the nonlinear loading situation. Since the DC link provides the energy to load during any unwanted situation due to non-linear load implementation, the compensation requirement amount is determined by DC link voltage. An ANN controller is required to control this activity properly. DC voltage v_{dc} should be maintained at a constant value to minimize the losses. The ANN is used to estimate the normalized weighting factor.

NBP-based $i \cos \emptyset$ control
The block diagram of this technique is presented in Fig. 3. At first, the load currents (i_{al}, i_{bl}, i_{cl}) and source voltages(v_{as}, v_{bs}, v_{cs}) are sensed. Then the direct current components ($i_{al} \cos \emptyset_{al}, i_{bl} \cos \emptyset_{bl}, i_{cl} \cos \emptyset_{cl}$) and the quadrature current components ($i_{al} \sin \emptyset_{al}, i_{bl} \sin \emptyset_{bl}, i_{cl} \sin \emptyset_{cl}$) are extracted by implementing $i \cos \emptyset$ technique[17–32]. After that these clustered weights are again processed through the NBP training mechanism. Here an updating of weight operation is done by an iterative method. As a result, a finely tuned weighted value of the active components ($w'_{alp}, w'_{blp}, w'_{clp}$) and reactive components ($w'_{alq}, w'_{blq}, w'_{clq}$) of the current is obtained. Then a filtered and tuned active component of weighting factor w_{lp} and the reactive component of weighting factor w_{lq} is generated. These weighting factors are not affected by noise, so, become more stable.

Extraction of weighted values of active load current and reactive load current component
The three-phase weights for the active components ($w'_{alp}, w'_{blp}, w'_{clp}$) and reactive components ($w'_{alq}, w'_{blq}, w'_{clq}$) are evaluated from the load current by NBP-based $i \cos \emptyset$ method. The extraction of weighted values and weight updating of the current components is presented in Fig. 4.

The weighted active components of current ($i_{alp}, i_{blp}, i_{clp}$) are generated as
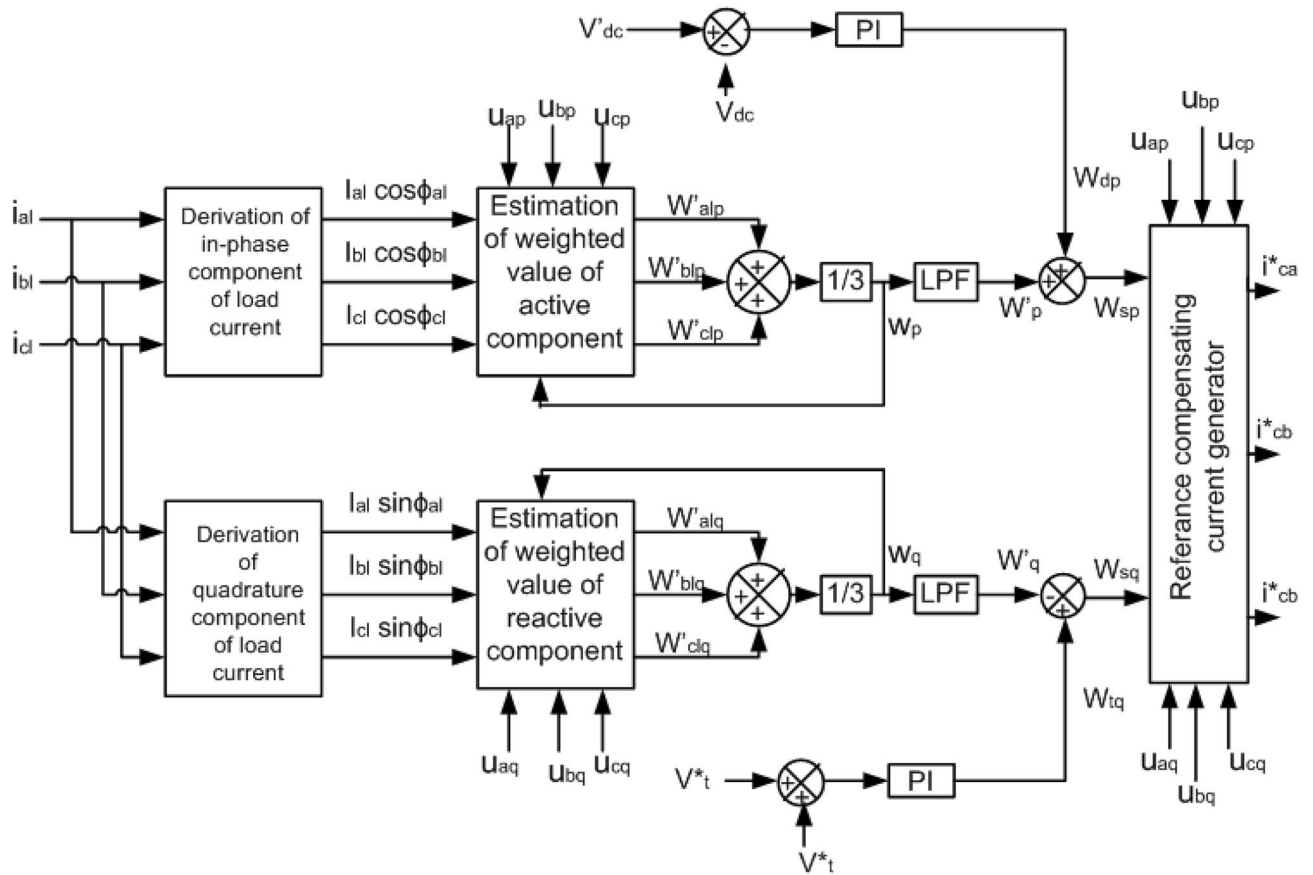
Figure 3. Block diagram of NBP based $i\cos\varnothing$ control technique.
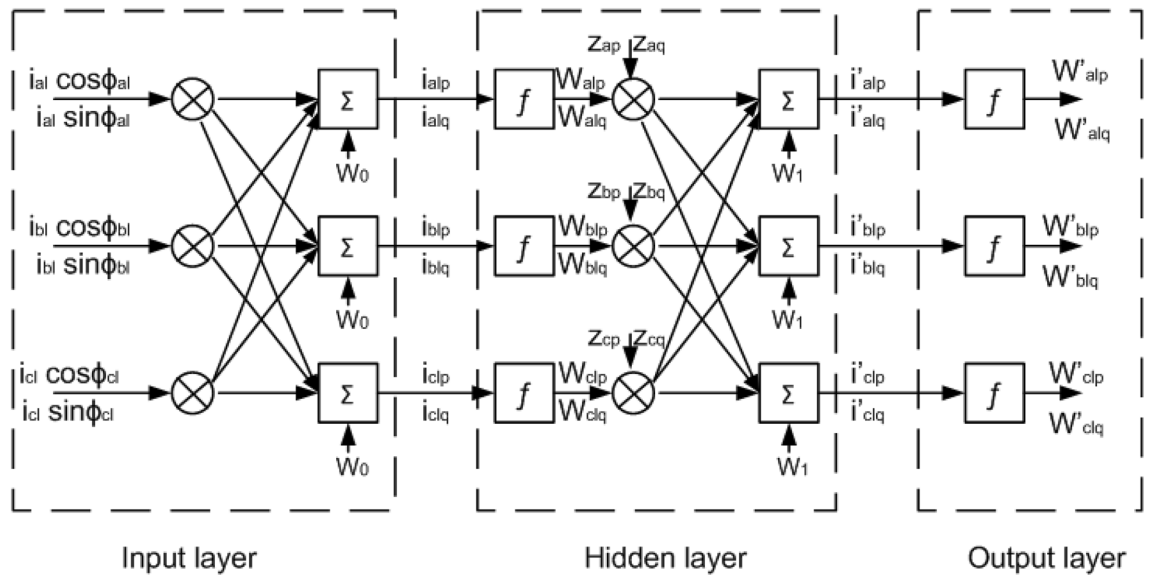

Figure 4. Extraction and updating weighted value using NBP technique.

$$\begin{bmatrix} i_{alp} \\ i_{blp} \\ i_{clp} \end{bmatrix} = w_0 + \begin{bmatrix} i_{al}\cos\varnothing_{al} & i_{bl}\cos\varnothing_{bl} & i_{cl}\cos\varnothing_{cl} \end{bmatrix} \begin{bmatrix} u_{ap} \\ u_{bp} \\ u_{cp} \end{bmatrix} \tag{10}$$

where w_0 is the initial weight. u_{ap}, u_{bp}, u_{cp} are unit voltage active components. The unit voltage active components are generated using the source voltages at PCC.

$$\begin{bmatrix} u_{ap} \\ u_{bp} \\ u_{cp} \end{bmatrix} = \frac{1}{v_t} \begin{bmatrix} v_{as} \\ v_{bs} \\ v_{cs} \end{bmatrix} \tag{11}$$

where v_t is the amplitude voltage evacuated as

$$v_t = \sqrt{\frac{2\left(v_{as}^2 + v_{bs}^2 + v_{cs}^2\right)}{3}} \tag{12}$$

The active current component ($i_{alp}, i_{blp}, i_{clp}$) are operated through an uninterrupted sigmoid function to get weights ($w_{alp}, w_{blp}, w_{clp}$) as

$$\begin{bmatrix} w_{alp} \\ w_{blp} \\ w_{clp} \end{bmatrix} = \begin{bmatrix} f\left(i_{alp}\right) \\ f\left(i_{blp}\right) \\ f\left(i_{clp}\right) \end{bmatrix} = 1 \div \begin{bmatrix} 1 + e^{-i_{alp}} \\ 1 + e^{-i_{blp}} \\ 1 + e^{-i_{clp}} \end{bmatrix} \tag{13}$$

These weighted signals $w_{alp}, w_{blp}, w_{clp}$ are processed through hidden layers. The results of this hidden layer are $i'_{alp}, i'_{blp}, i'_{clp}$, that are expressed as

$$\begin{bmatrix} i'_{alp} \\ i'_{blp} \\ i'_{clp} \end{bmatrix} = w_1 + \begin{bmatrix} Z_{ap} & Z_{bp} & Z_{cp} \end{bmatrix} \begin{bmatrix} w_{alp} \\ w_{blp} \\ w_{clp} \end{bmatrix} \tag{14}$$

where w_1 is the earliest weight of the invisible layer, and Z_{ap}, Z_{bp}, Z_{cp} are revised weights of the active current component of each phase.

The revised weight signals Z_{ap}, Z_{bp}, Z_{cp} can be extracted as given in (15). Where $w'_{alp}, w'_{blp}, w'_{clp}$ are fundamental weights of the active components of load current. w_p is the mean weight. μ is the rate of learning. In this work μ is selected as 0.6 within a range of 0–1. $f'\left(i'_{alp}\right), f'\left(i'_{blp}\right)$ and $f'\left(i'_{clp}\right)$ are the first derivatives of i'_{alp}, i'_{blp} and i'_{clp} respectively. w_{alp}, w_{blp} and w_{clp} are the outputs of the hidden layer.

$$\begin{bmatrix} Z_{ap} \\ Z_{bp} \\ Z_{cp} \end{bmatrix} = w_p + \left\{ \mu \begin{bmatrix} w_p - w'_{alp} & w_p - w'_{blp} & w_p - w'_{clp} \end{bmatrix} \begin{bmatrix} w_{alp} \\ w_{blp} \\ w_{clp} \end{bmatrix} + \begin{bmatrix} f'\left(i'_{alp}\right)^H \\ f'\left(i'_{blp}\right)^H \\ f'\left(i'_{clp}\right)^H \end{bmatrix} \right\} \delta \tag{15}$$

i'_{alp}, i'_{blp} and i'_{clp} values are extracted and then processed through the sigmoid function to get w'_{alp}, w'_{blp} and w'_{clp}

$$\begin{bmatrix} w'_{alp} \\ w'_{blp} \\ w'_{clp} \end{bmatrix} = \begin{bmatrix} f\left(i'_{alp}\right) \\ f\left(i'_{blp}\right) \\ f\left(i'_{clp}\right) \end{bmatrix} = \begin{bmatrix} 1 + e^{-i'_{alp}} \\ 1 + e^{-i'_{blp}} \\ 1 + e^{-i'_{clp}} \end{bmatrix} \tag{16}$$

The average weighted value w_p is calculated by talking mean such as

$$w_p = \frac{w'_{alp} + w'_{blp} + w'_{clp}}{3} \tag{17}$$

Then it is processed through a LPF (low pass filter). The result of the LPF is w'_p.
Similarly, the weighted reactive component current i_{alq}, i_{blq} and i_{clq} are generated as

$$\begin{bmatrix} i_{alq} \\ i_{blq} \\ i_{clq} \end{bmatrix} = w_0 + \begin{bmatrix} i_{al} \sin \emptyset_{al} & i_{bl} \sin \emptyset_{bl} & i_{cl} \sin \emptyset_{cl} \end{bmatrix} \begin{bmatrix} u_{aq} \\ u_{bq} \\ u_{cq} \end{bmatrix} \tag{18}$$

where u_{aq}, u_{bq} and u_{cq} are unit voltage reactive component and can be derived as

$$\begin{bmatrix} u_{aq} \\ u_{bq} \\ u_{cq} \end{bmatrix} = \frac{1}{\sqrt{3}} \begin{bmatrix} 0 & u_{bp} & u_{cp} \\ 3u_{ap} & u_{bp} & -u_{cp} \\ -3u_{ap} & 3u_{bp} & -u_{cp} \end{bmatrix} \tag{19}$$

The reactive component of current i_{alq}, i_{blq} and i_{clq} are operated through uninterrupted sigmoid function to get w_{alq}, w_{blq} and w_{clq}.

$$\begin{bmatrix} w_{alq} \\ w_{blq} \\ w_{clq} \end{bmatrix} = \begin{bmatrix} f\left(i_{alq}\right) \\ f\left(i_{blq}\right) \\ f\left(i_{clq}\right) \end{bmatrix} = 1 \div \begin{bmatrix} 1 + e^{-i_{alq}} \\ 1 + e^{-i_{blq}} \\ 1 + e^{-i_{clq}} \end{bmatrix} \tag{20}$$

These weighted signals w_{alq}, w_{blq} and w_{clq} are processed through hidden layers. The output of this hidden layer are i'_{alq}, i'_{blq} and i'_{clq}, such as

$$\begin{bmatrix} i'_{alq} \\ i'_{blq} \\ i'_{clq} \end{bmatrix} = w_1 + \begin{bmatrix} Z_{aq} & Z_{bq} & Z_{cq} \end{bmatrix} \begin{bmatrix} w_{alq} \\ w_{blq} \\ w_{clq} \end{bmatrix} \tag{21}$$

Here Z_{aq}, Z_{bq} and Z_{cq} are revised weights of the reactive current component of each phase and can be represented as shown in (22). where w'_{alq}, w'_{blq} and w'_{clq} are fundamental weighted amplitudes of reactive load current components. w_q is the mean weight. μ is the rate of learning. $f'\left(i'_{alq}\right)$, $f'\left(i'_{blq}\right)$ and $f'\left(i'_{clq}\right)$ are the first derivatives of i'_{alq}, i'_{blq} and i'_{clq} respectively. w_{alq}, w_{blq} and w_{clq} are the outputs of the hidden layer.

$$\begin{bmatrix} Z_{aq} \\ Z_{bq} \\ Z_{cq} \end{bmatrix} = w_q + \left\{ \mu \begin{bmatrix} w_q - w'_{alq} & w_q - w'_{blq} & w_q - w'_{clq} \end{bmatrix} \begin{bmatrix} w_{alq} \\ w_{blq} \\ w_{clq} \end{bmatrix} + \begin{bmatrix} f'\left(i'_{alq}\right)^H \\ f'\left(i'_{blq}\right)^H \\ f'\left(i'_{clq}\right)^H \end{bmatrix} \right\} \delta \tag{22}$$

The values i'_{alq}, i'_{blq} and i'_{clq} are extracted and processed through the uninterrupted sigmoidal function to generate the weighted signals w'_{alq}, w'_{blq} and w'_{clq}, such as

$$\begin{bmatrix} w'_{alq} \\ w'_{blq} \\ w'_{clq} \end{bmatrix} = \begin{bmatrix} f\left(i'_{alq}\right) \\ f\left(i'_{blq}\right) \\ f\left(i'_{clq}\right) \end{bmatrix} = \begin{bmatrix} 1 + e^{-i'_{alq}} \\ 1 + e^{-i'_{blq}} \\ 1 + e^{-i'_{clq}} \end{bmatrix} \tag{23}$$

The average weighted value of w_q is calculated by talking mean, such as

$$w_q = \frac{w'_{alq} + w'_{blq} + w'_{clq}}{3} \tag{24}$$

Then it is processed through a LPF. The output of the LPF is w'_q.

Evaluation of active reference component

The error in DC voltage v_{dc} can be evaluated by taking the difference of sensed DC voltage v_{dc} from DC reference voltage v_{dc}^*. This error signal is processed through PI controller, such as

$$w_{dp} = k_{dp}v_{dc} + k_{ip}\int v_{dc}dt \tag{25}$$

The active weighted reference current component w_{sp} is obtained by adding the average magnitude of active load current component w'_p and the output of the PI controller w_{dc}.

$$w_{sp} = w_{dp} + w'_p \tag{26}$$

Evaluation of active reference component

The error signal in AC voltage can be evaluated by taking the difference of sensed AC voltage v_t from AC reference voltage v_t^*. This error signal is processed through PI controller, such as

$$w_{tq} = k_{tq}v_t + k_{iq}\int v_t dt \tag{27}$$

The reactive weighted reference current component w_{sq} is derived by subtracting the mean magnitude of reactive load component w'_q from the output result of PI controller w_{tq}.

$$w_{sq} = w_{tq} - w'_q \tag{28}$$

Evaluation of reference compensating current components

The three-phase active reference current components i_{cap}, i_{cbp} and i_{ccp} are predicted by multiplying matrix of unit voltage active components u_{ap}, u_{bp}, u_{cp} with the total active weighted current component w_{sp}.

$$\begin{bmatrix} i_{cap} \\ i_{cbp} \\ i_{ccp} \end{bmatrix} = w_{sp} \begin{bmatrix} u_{ap} \\ u_{bp} \\ u_{cp} \end{bmatrix} \tag{29}$$

Similarly, the three-phase reactive reference current components i_{caq}, i_{cbq} and i_{ccq} are estimated by multiplying unit voltage reactive components u_{aq}, u_{bq}, u_{cq} matrix with the total reactive weighted current component w_{sq}.

$$\begin{bmatrix} i_{caq} \\ i_{cbq} \\ i_{ccq} \end{bmatrix} = w_{sq} \begin{bmatrix} u_{aq} \\ u_{bq} \\ u_{cq} \end{bmatrix} \tag{30}$$

The reference compensating current i_{ca}^*, i_{cb}^* and i_{cc}^* are realized by adding these active and reactive components of reference current, such as

$$\begin{bmatrix} i_{ca}^* \\ i_{cb}^* \\ i_{cc}^* \end{bmatrix} = \begin{bmatrix} i_{cap} \\ i_{cbp} \\ i_{ccp} \end{bmatrix} + \begin{bmatrix} i_{caq} \\ i_{cbq} \\ i_{ccq} \end{bmatrix} \tag{31}$$

Then the reference current for compensation (i_{ca}^*, i_{cb}^*, i_{cc}^*) are compared with the compensating current. The result of this comparison generates signal for modulation to produce the firing pulses for the semiconductor devices of the MLI.

Generation of triggering signals for the semiconductor switches

In the present work the multi-carrier based PWM, called phase-shifted pulse width modulation (PS-PWM) is applied[33,34]. The reference current for compensation (i_{ca}^*, i_{cb}^*, i_{cc}^*) are correlated here with the compensation currents of the SAPF (i_{ca}, i_{cb}, i_{cc}). Now the difference is provided to the PWM block to produce the firing pulse signals for the semiconductor devices of the MLI, where the deference of the compensating current to the reference current is compared with triangular carrier waves. There is a 3 K number of carriers required, and these carriers are shifted by phase to develop firing pulses for each switch in the MLI. The block diagram of the PWM technique is presented in Fig. 5. Because of this, the power-sharing between the modules or cells becomes systematic. The diagram in Fig. 6 represents the close loop control strategy of the SAPF. In this diagram the functioning of the total control system is represented including the ANN (NBP-based $i\cos\varnothing$ technique) based reference current generator, triggering pulse generator and the SAPF as a whole.

Results of simulation

The simulation model for the SAPF with different control strategies is designed in MATLAB/SIMULINK using the power system toolbox in it. The proposed SAPF is investigated under various load conditions. During the observation, the grid voltage is kept ideal. The parameter specification is presented in Table 1. In the simulation model, a nonlinear load is considered to be connected to the grid. This nonlinear load is consisting of an unrestrained rectifier bridge with an inductive load. The magnitude of resistance R is equal to 20Ω and that of the inductance L is equal to 20 mH. The SAPF is introduced after 0.1 s. Figure 7 shows the working behaviour of the active filter under this balanced non-linear loading condition. The load current i_l, compensating current i_c, source current i_s, source voltage v_s, and DC link voltage v_{dc} are presented respectively. The THD of the grid source current is realized to be 21.56% before the initialization of the active filter as shown in Fig. 8. But, it reduced to 1.77% after the initialization of the SAPF as shown in Fig. 9.
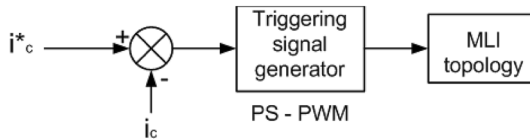

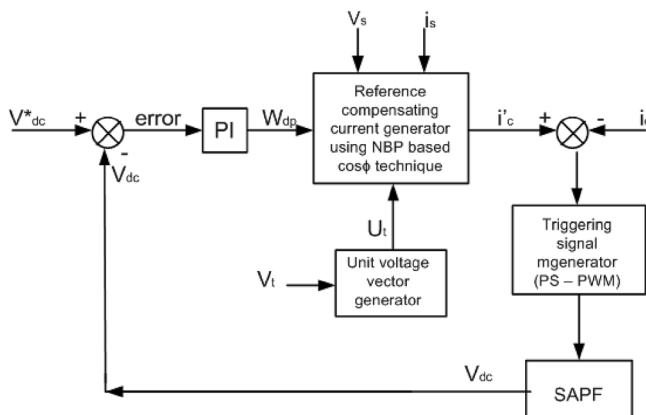**Figure 5.** Block Diagram for the PWM Technique application.

Figure 6. Control strategy block diagram for the SAPF.

Sl. no.	System parameters	Specification
1	Grid voltage 'V_s' [line–line]	415 V
2	Switching frequency 'f_s'	50 Hz
3	DC link capacitance 'C_{dc}'	2200 μF
4	Non-linear load [first]	Uncontrolled rectifier bridge with RL load R = 20 Ω and L = 20 mH
5	Non-linear load [second]	Uncontrolled rectifier bridge with RL load R = 25 Ω and L = 25 mH
6	Unbalanced 3-phase RL load	R_1= 30 Ω, L_1= 10 mH R_2= 10 Ω, L_2= 20 mH R_3= 20 Ω, L_3= 20 mH
7	Single-phase RL load	R = 30 Ω, L = 20 mH

Table 1. Parameter specification for simulation.
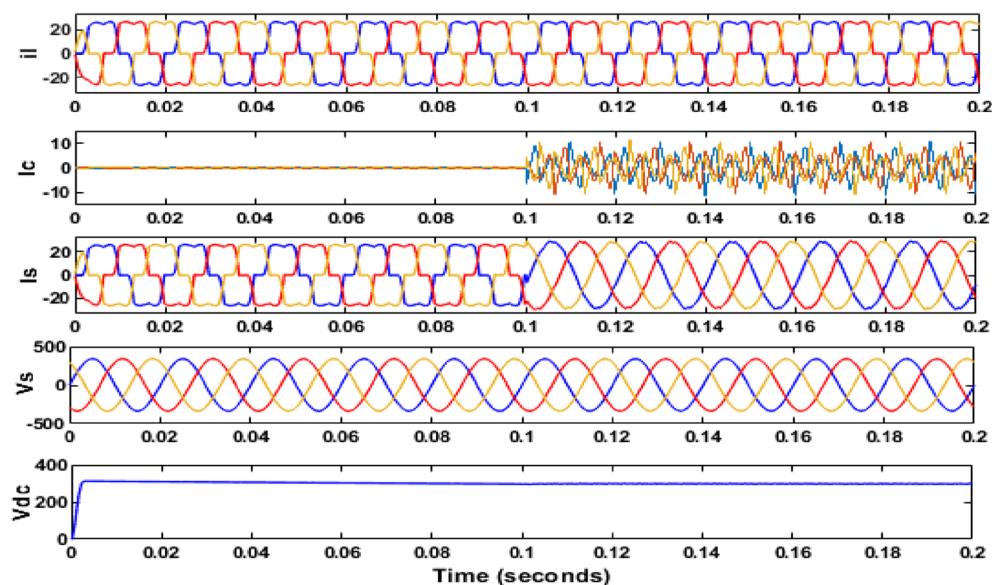
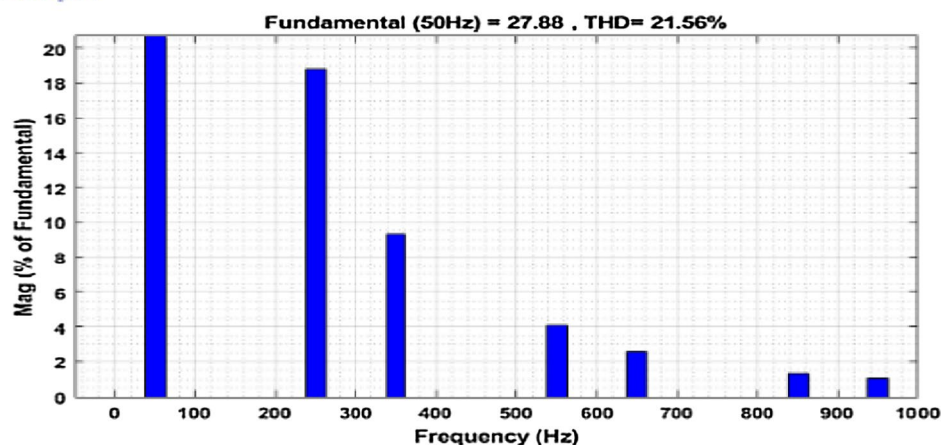**Figure 7.** Operating characteristic of proposed SAPF during non-linear loading condition.

Figure 8. THD of grid current 'i_s' before compensation in nonlinear loading condition.
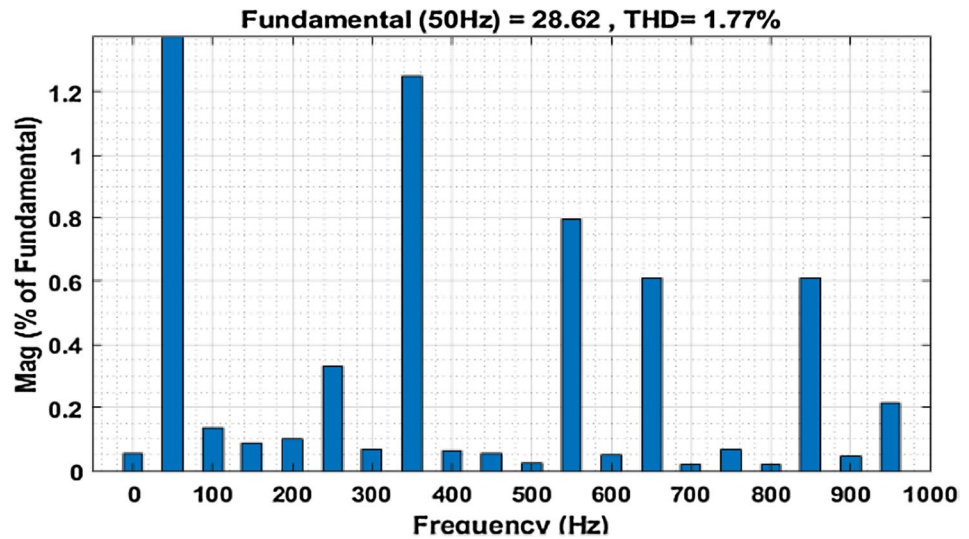
9

Figure 9. THD of grid current '*i*$_s$' after compensation in nonlinear loading condition.

Then the system performance is observed under a variable loading condition. After 0.2 s a step variation is done in the load. A balanced non-linear load is added parallel to the present load. The observation result is revealed in Fig. 10. The THD value in the grid source current without filtering is realized to be 22.02% as shown in Fig. 11. It reduced to 2.49% after filtering as depicted in Fig. 12. After that the system performance is observed for an unbalanced loading condition. Here a single-phase inductive RL load is connected between two phases, those are phase 'a' and phase 'b', where R = 30Ω and L = 20 mH. Here the active filter is initiated at 0.1 s and the variation in load is done at 0.2 s. The performance behavior is shown in the Fig. 13. Figures 14 and 15 show the FFT result of the unbalanced loading situation before and after filtering respectively. It is found the before filtering the THD value was 13.58%, which reduces to 1.61% after filtering.

Then the system is observed for an unbalanced loading condition, where an unbalanced three-phase inductive RL load is added parallel to the present non-linear load system. The SAPF is introduced at 0.1 s the unbalanced inductive load is added parallel to the previous load system at 0.2 s. The Fig. 16 shows the performance at this
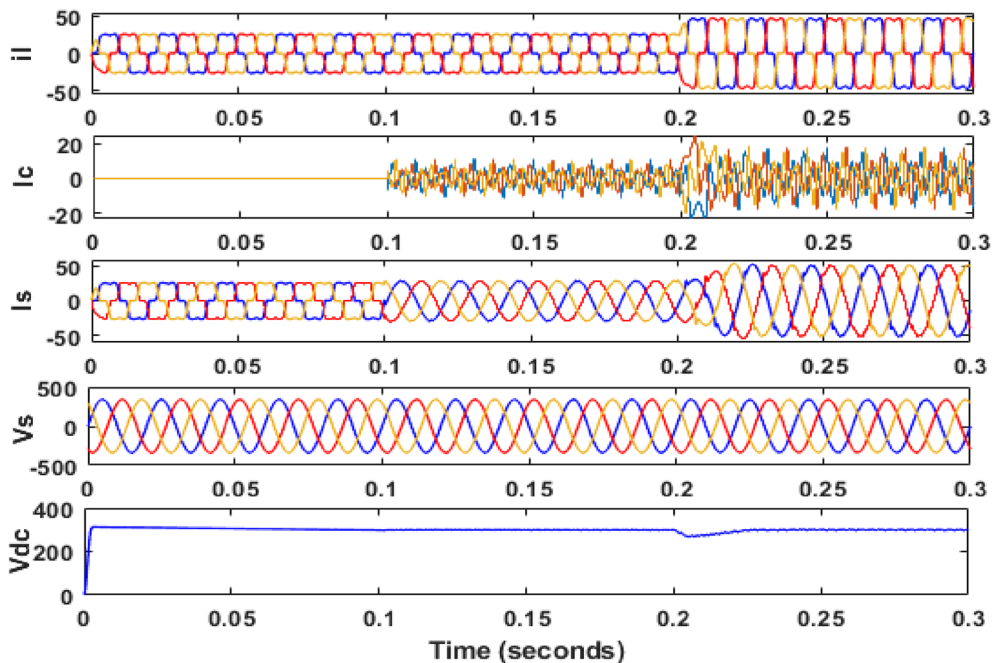

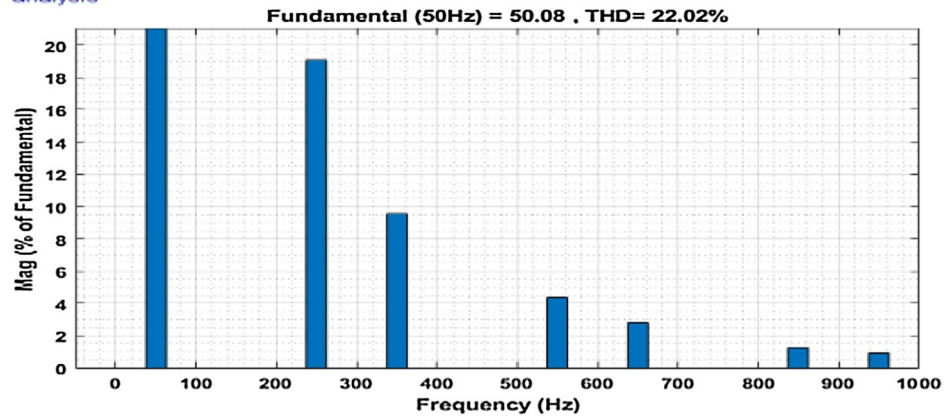**Figure 10.** Performance characteristic of proposed SAPF with a step changing non-linear load.

Figure 11. THD of grid current 'i_s' before compensation during step changed non-linear load.
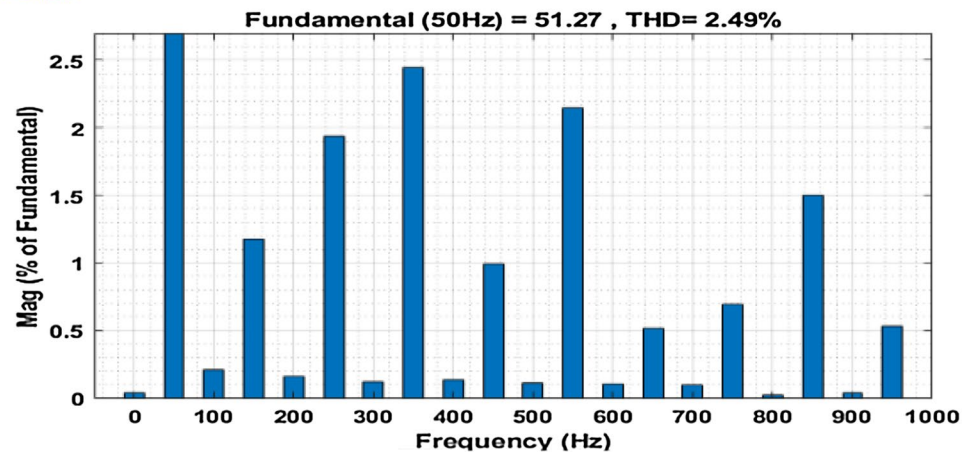

Figure 12. THD of grid current 'i_s' after compensation during step changed non-linear load.

condition. Figures 17 and 18 show the FFT result for this unbalanced loading condition before and after initialization of filter respectively. The result shows the THD value of the grid source current without compensation is 14.48%, which minimized to 1.24% after compensation.

Comparison with ($i_d - i_q$) and $i \cos \emptyset$ control techniques

Here the operating characteristic of the proposed SAPF with the NBP-based $i \cos \emptyset$ technique is compared with the other two control techniques. These are two conventional techniques ($i_d - i_q$ control technique and $i \cos \emptyset$ control technique). The observations are taken in each loading condition and compared with the proposed NBP-based $i \cos \emptyset$ technique. The comparison between these three control techniques for the SAPF is presented in Table 2.

$i_d - i_q$ control technique

The performance of the SAPF using $i_d - i_q$ control technique is also examined. The THD of the load current i_l is 21.56%, the THD of the grid source current i_s is reduced to 4.91%. When a step change in load is done, it is observed that the THD value of source current is diminished from 22.02 to 4.97% after initiation of SAPF. When the single-phase RL load is connected in between phase 'a' and phase 'b' the THD value is reduced from 13.58 to 4.25%. In case of unbalanced three-phase inductive load, the THD value of source current comes down from 14.48 to 4.78% after filtration.

$i \cos \emptyset$ control technique

The performance of the SAPF using $i \cos \emptyset$ control method is examined. The THD of the load current i_l is 21.56%, and the THD of the grid source current i_s is reduced to 3.86%. When a step change in load is done it is detected that the THD value of source current is diminished from 22.02 to 3.95% after compensation. When the single-phase RL load is connected in between the phases 'a' and 'b' the THD value is reduced from 13.58 to 3.19% in
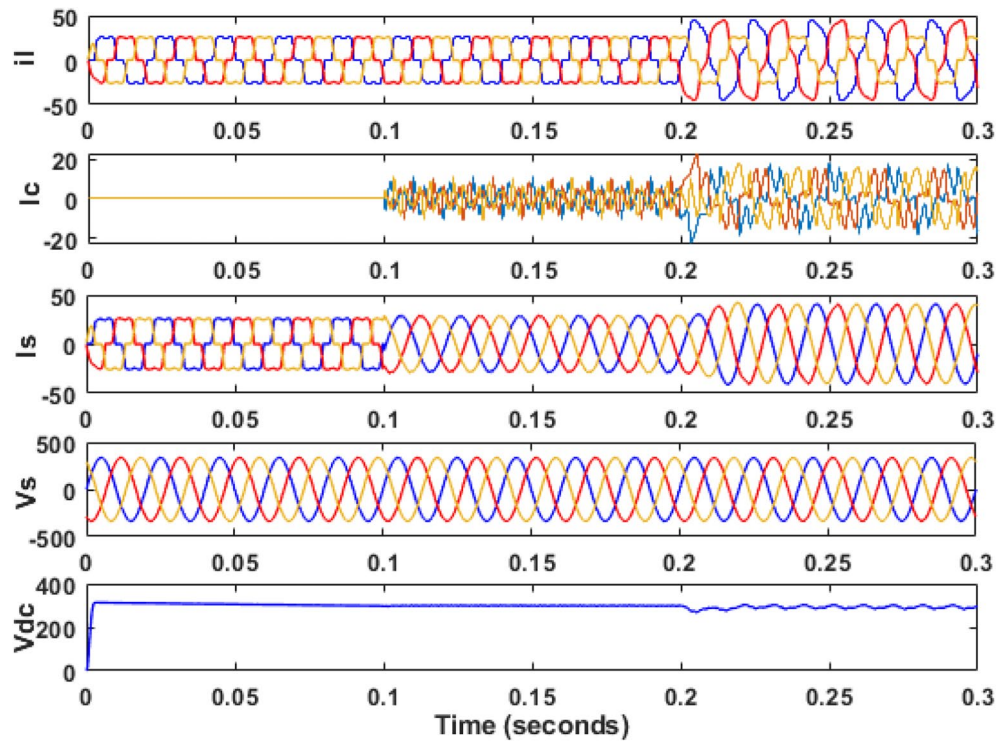
Figure 13. Performance characteristic of proposed SAPF with addition of a single-phase inductive load in between line 'a' and 'b'.
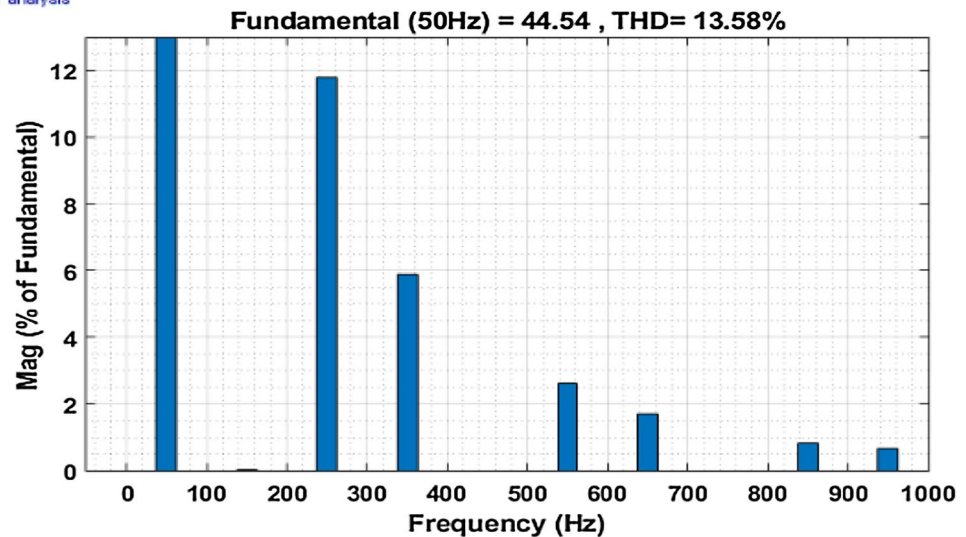

Figure 14. THD of grid current 'i_s' before compensation with addition of a single-phase inductive load in between line 'a' and 'b'.

case of a three-phase unbalanced inductive load the THD value of source current comes down from 14.48 to 3.52% after filtration.

The source current harmonic elimination relies upon the active and reactive components of the load current. And, for PCC voltage balancing the DC-link capacitance–voltage management is important. The voltage management can be done by using the weights of the load components, which are extracted by an LPF. These weighted values are not updated in the classical methods like $i_d - i_q$ and $i\cos\emptyset$ control techniques. But these weights are updated in the NBP-based $i\cos\emptyset$ method. So, the voltage regulation becomes more effective. On the basis of the THD value of source current, the NBP-based $i\cos\emptyset$ technique is more effective for our proposed SAPF to eliminate the harmonics.
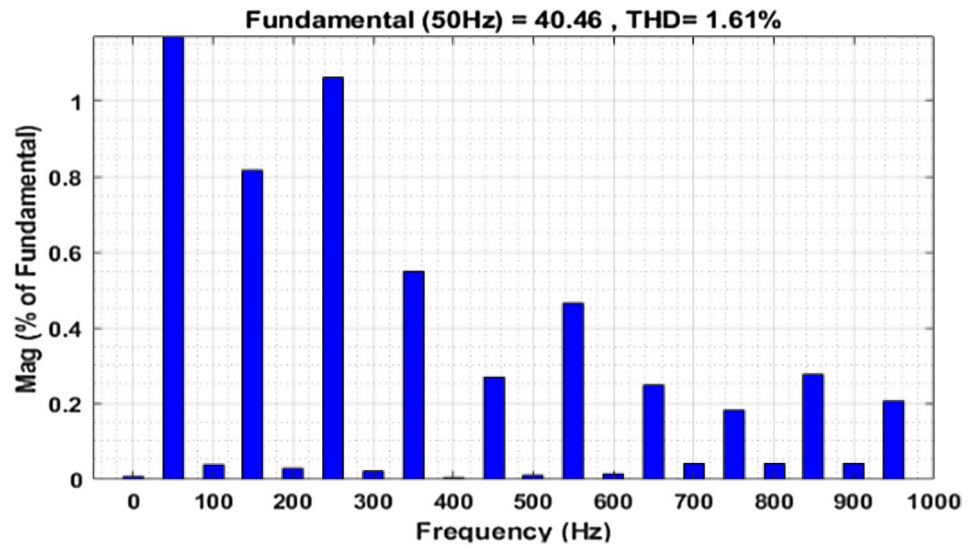
Figure 15. THD of grid current 'i_s' after compensation with addition of a single-phase inductive load in between line 'a' and 'b'.
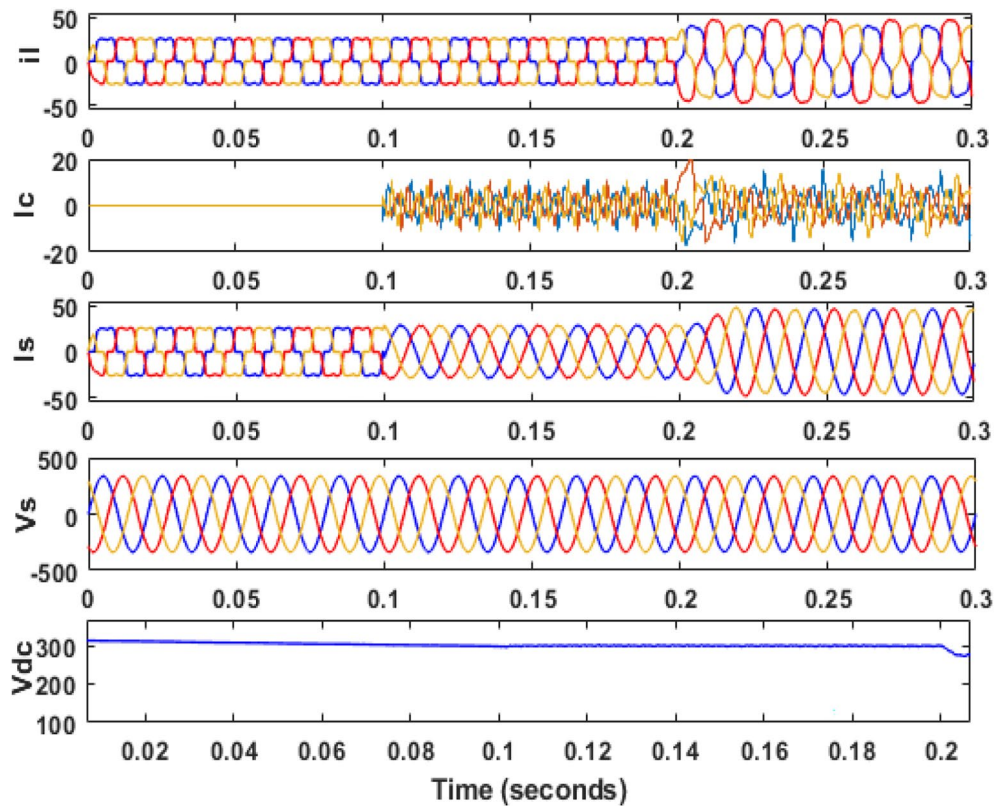
Figure 16. Performance characteristic of proposed SAPF with addition of an unbalanced three-phase load.

The DC-link capacitance voltage performance is also better in the case of the NBP-based $i \cos \emptyset$ method than in the other two methods. It is noticed that the SAPF with NBP-based $i \cos \emptyset$ gives results with less harmonics with reduced DC-link capacitance voltage. There are some other advantages such as reduced MLI rating, and low DC link capacitor stress. So, it is concluded that the SAPF operating with the NBP-based $i \cos \emptyset$ control technique is better than the conventional techniques.

Figure 17. THD of grid current 'i_s' before compensation with addition of an unbalanced three-phase RL load.

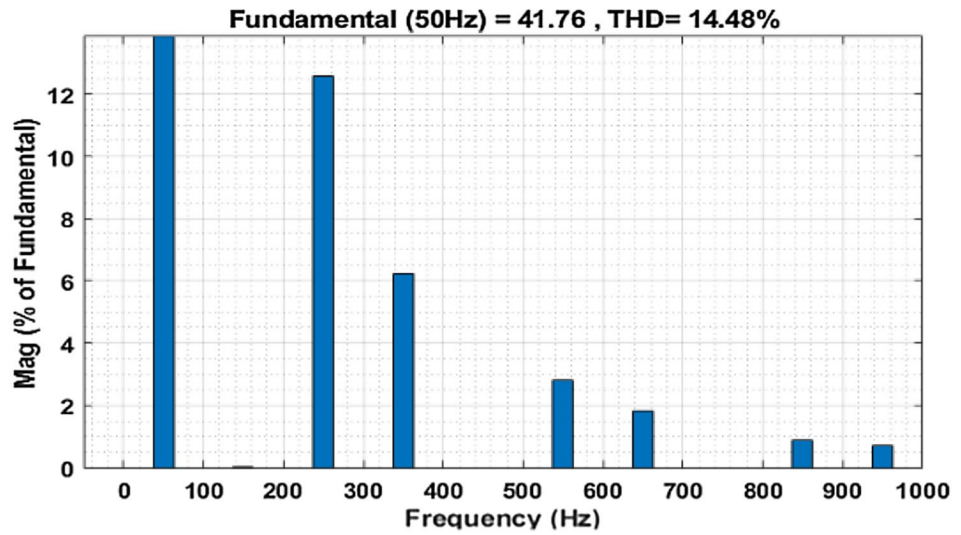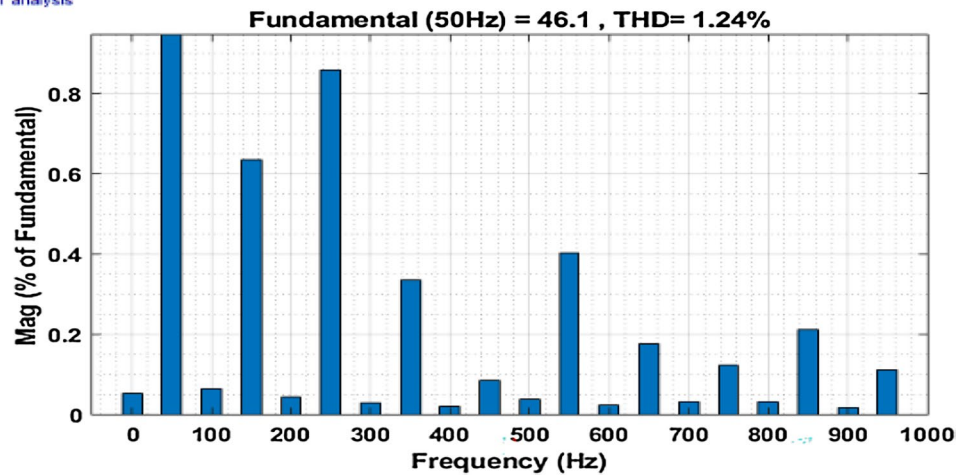**Figure 18.** THD of grid current 'i_s' after compensation with addition of an unbalanced three-phase RL load.

Control technique	Time invariant non-linear load		Step change in non-linear load		Addition of 1-phase RL load between phase 'a' and 'b'		Addition of 3-phase RL imbalanced load	
	Before filtering	After filtering	Before filtering	After filtering	Before filtering	After filtering	Before filtering	After filtering
$i_d - i_q$	21.56%	4.91%	22.02%	4.97%	13.58%	4.25%	14.48%	4.78%
$i \cos \emptyset$	21.56%	3.86%	22.02%	3.95%	13.58%	3.19%	14.48%	3.52%
NBP-based $i \cos \emptyset$	21.56%	1.77%	22.02%	2.49%	13.58%	1.61%	14.48%	1.24%

table 2. Comparison of control techniques based on THD% in source current in different loading condition.

Real-time implementation and experimental result of the proposed SAPF

The implementation of the hardware of the suggested SAPF topology is presented in Fig. 19. The hardware arrangement consists of the suggested cascaded MLI incorporated of three modules. The modules are cascaded through a transformer with filter inductors connected in series. The setup also includes a single DC link capacitor, voltage sensor, current sensor, 3-phase uncontrolled rectifier bridge, FPGA module, etc.

The reference DC-link capacitance voltage is predetermined at 160 V. For recording the experimental results, a power analyzer with six-channels is connected. The hardware arrangement is probed under balanced invariable
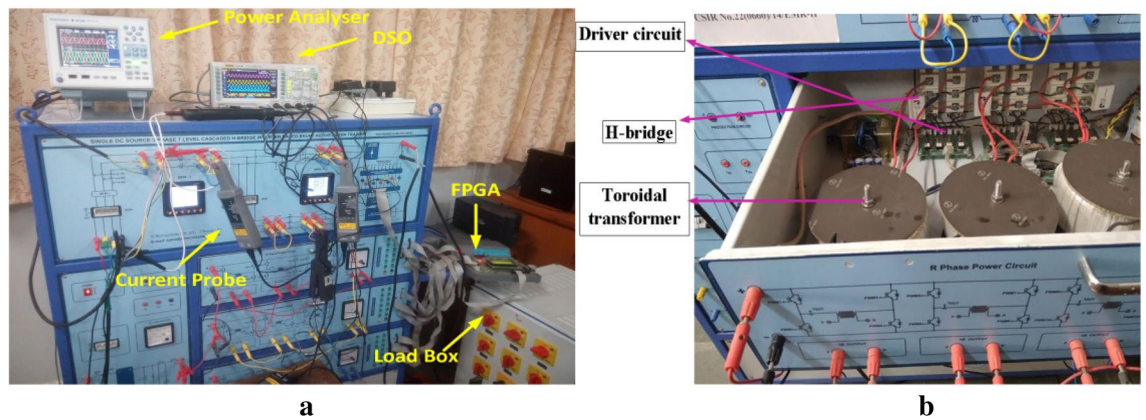
Figure 19. Experimental set up of the proposed system: (**a**) whole system, (**b**) connection of transformer in SAF for phase-A.

source voltage condition. The SAPF operation is examined under balanced non-linear loading steady state circumstances is presented in Fig. 20. The supply voltage 'v_s', grid supply current 'i_s', load current 'i_l', and compensating current 'i_c' of a single phase is shown here.

Figure 21 shows the operational behavior of the SAPF under the transient condition. Here the supply voltage 'v_s', supply current 'i_s', load current 'i_l', and compensating current 'i_c' before and after reimbursement is shown. From this it is clearly understood that the harmonics present in the supply current is removed and it turns into sinusoidal after filtration. This operation is done with a smooth and slight variation in DC link capacitance voltage. The FFT result of the working of the SAPF is presented in Figs. 22 and 23. These show that the THD of supply current under non-linear load in balanced condition, before compensation is 23.55%, and it reduced to 2.73% after compensation. Figure 24 shows the operational characteristic of the SAPF during a sudden step changed load. Here also the v_{dc} varies smoothly to generate required compensating current and settles soon. The filter operates very efficiently at the transient. The performance under unbalanced loading condition (where a single-phase inductive (RL) load is connected between line 'a' and 'b' at PCC) is presented in Fig. 25. The filter seems to be very effective for unbalanced loading condition also.

The performance characteristic of SAPF under unbalanced load (where a three-phase unbalanced inductive load is connected in parallel at the PCC) is presented in Fig. 26. Where (a) shows the characteristics before compensation and (b) shows the characteristic after compensation. Figures 27 and 28 represent the FFT result of the source current under unbalanced load, where it is found that the THD of supply current is 25.71% before compensation, and it is reduced to 1.65% after compensation.
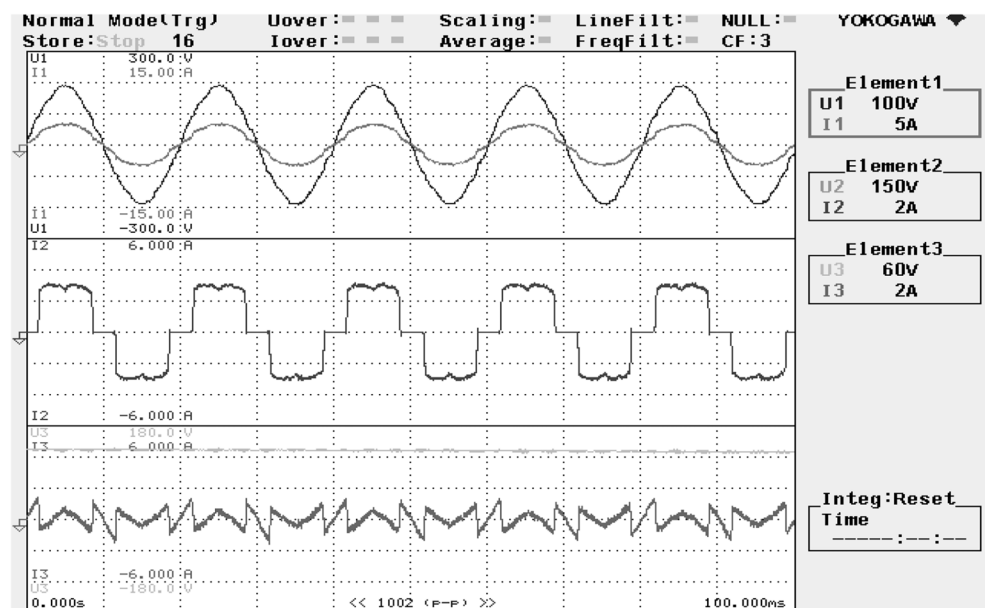

Figure 20. SAPF performance under steady state condition.
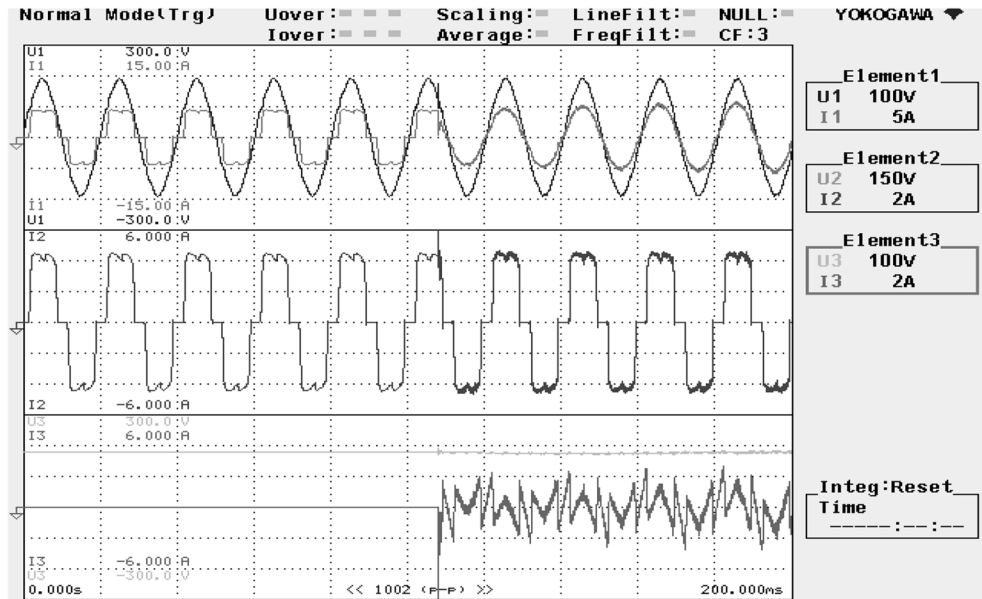
Figure 21. SAPF performance under transient condition.
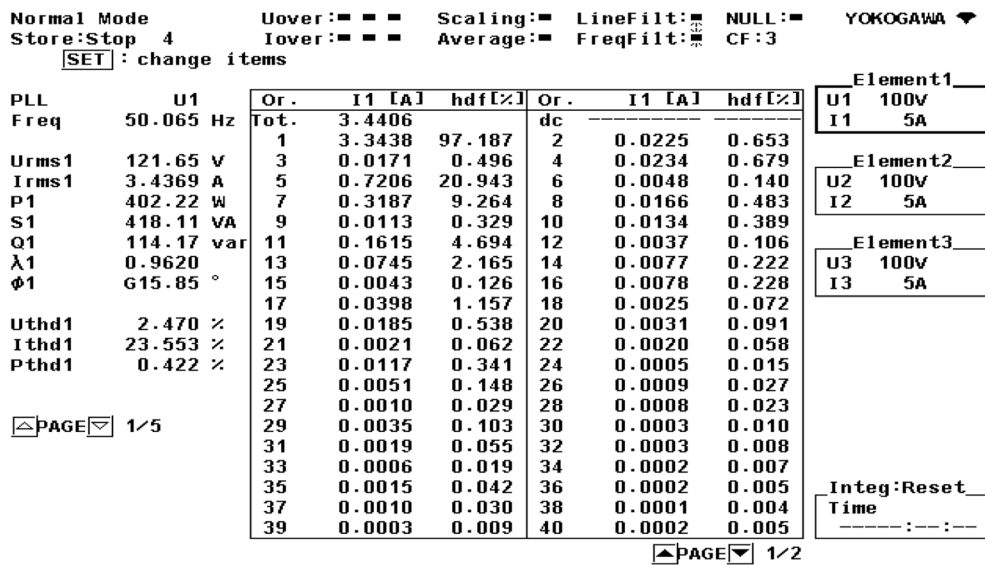
Figure 22. FFT result of the supply current under balanced load, before compensation.

Conclusion

In this paper the effectiveness of proposed NBP-based $i\cos\emptyset$ technique is compared with another two classical control techniques for power quality improvement on cascaded MLI based shunt active power filter. The harmonic current removal by the recommended control technique found to be more accurate compared to other control techniques discussed in the literature. The reference compensating current generation is done by using NBP-based $i\cos\emptyset$ method. As this control technique is having a feedback system, it can produce a precise weighting factor. So, this controller is very effective to reduce harmonics with less amount of voltage variation at DC link capacitor. From the simulation and experimental hardware result it is clear that, the recommended technique is more efficient than $i_d - i_q$ method and $i\cos\emptyset$ method to eliminate the harmonics in balanced and unbalanced non-linear loading condition.
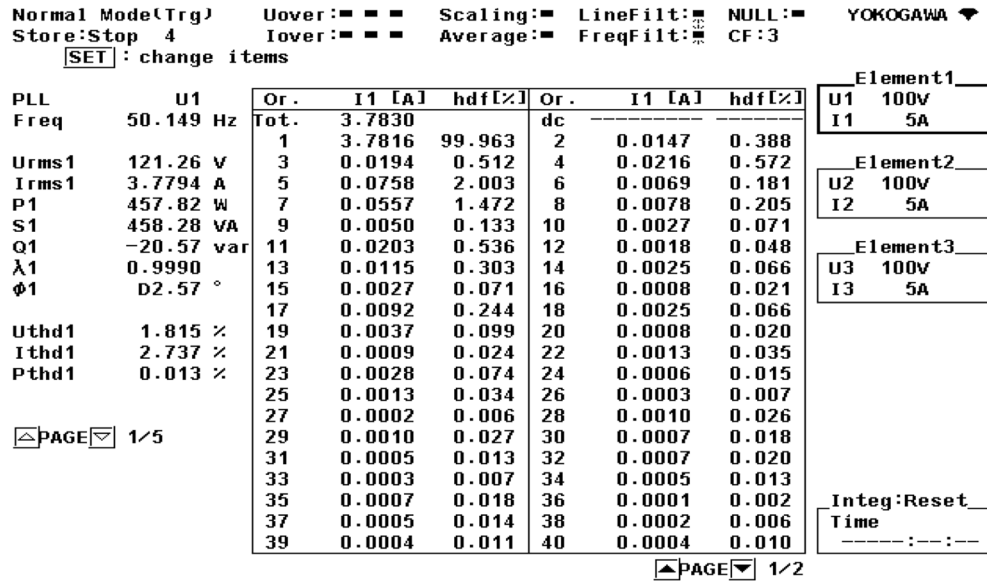
Figure 23. FFT result of the supply current under balanced load, after compensation.

Figure 24. SAPF Performance under step variation in non-linear load.
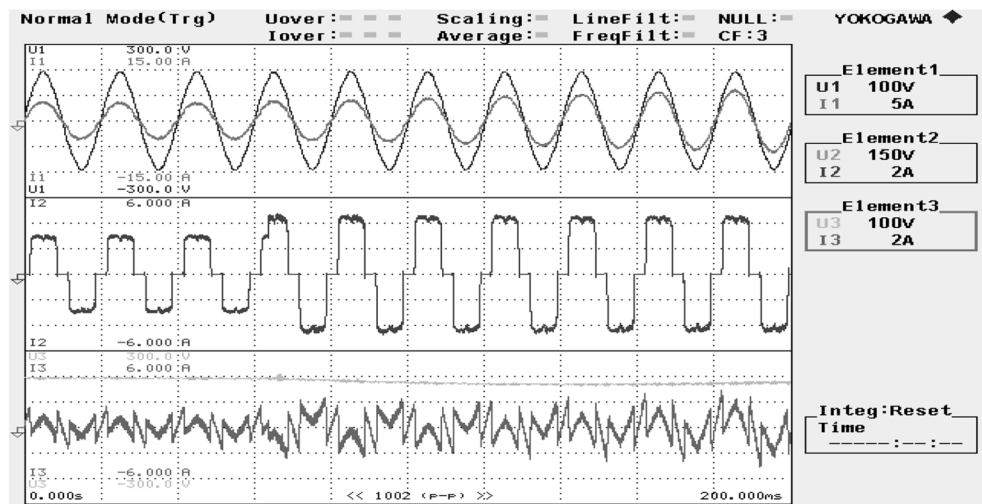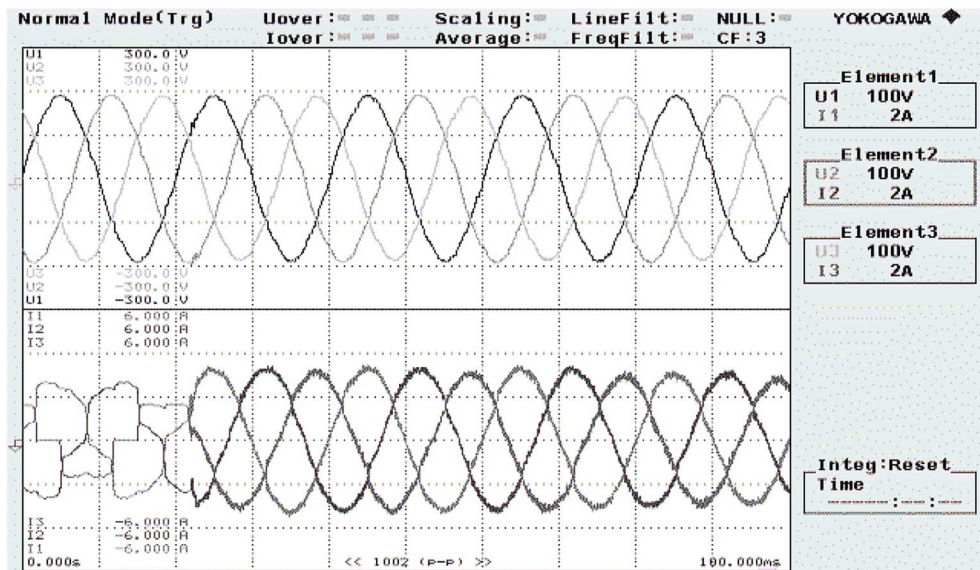
Figure 25. SAPF performance under unbalanced inductive load (single-phase RL load connected between phase 'a' and 'b' at PCC).
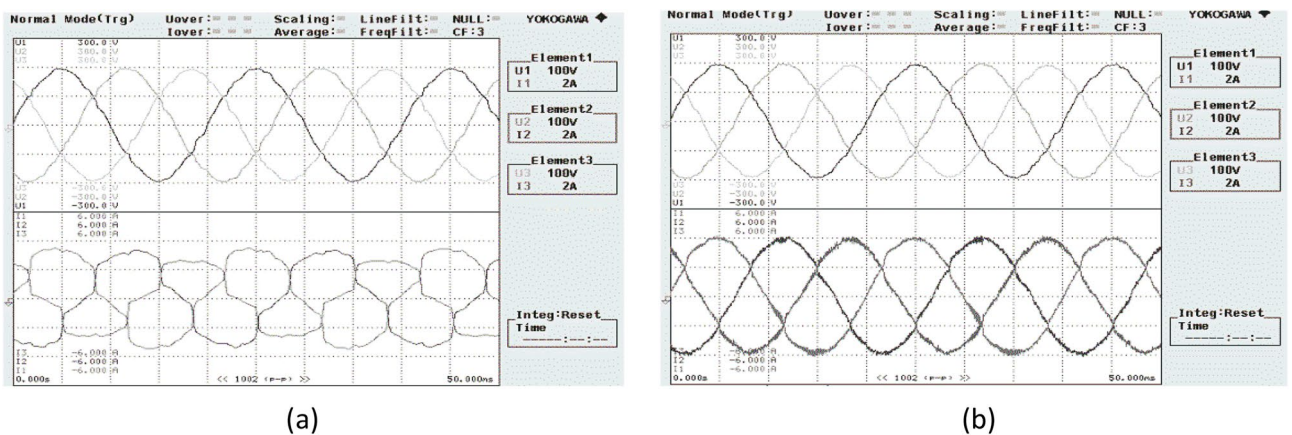

(a)

(b)

Figure 26. SAPF Performance under unbalanced load (three-phase load connected at PCC). (**a**) Before compensation and (**b**) after compensation.
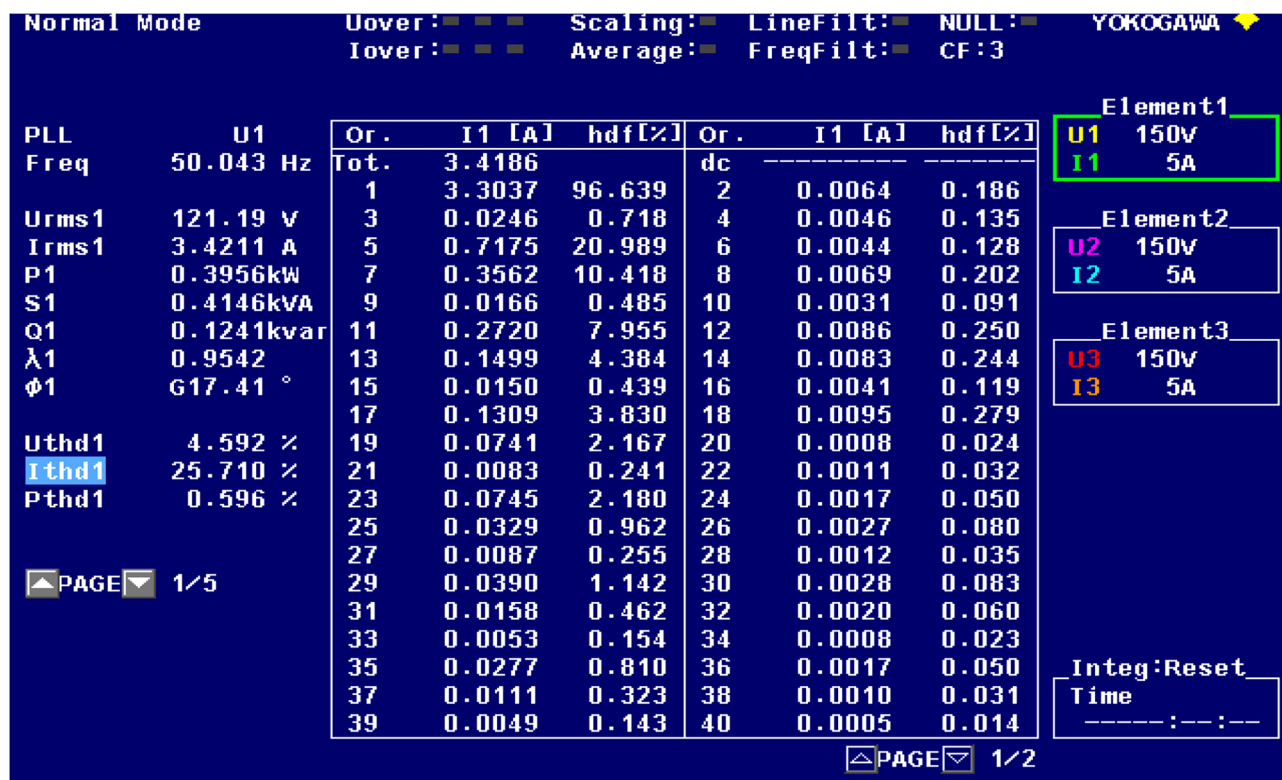
Normal Mode   Uover:■ ■ ■   Scaling:■   LineFilt:■   NULL:■   YOKOGAWA
   Iover:■ ■ ■   Average:■   FreqFilt:■   CF:3

PLL   U1
Freq   50.043 Hz

Urms1   121.19 V
Irms1   3.4211 A
P1   0.3956kW
S1   0.4146kVA
Q1   0.1241kvar
λ1   0.9542
φ1   G17.41 °

Uthd1   4.592 %
Ithd1   25.710 %
Pthd1   0.596 %

PAGE 1/5

Element1: U1 150V, I1 5A
Element2: U2 150V, I2 5A
Element3: U3 150V, I3 5A
Integ:Reset Time -----:--:--

Or.	I1 [A]	hdf[%]	Or.	I1 [A]	hdf[%]
Tot.	3.4186		dc	------	------
1	3.3037	96.639	2	0.0064	0.186
3	0.0246	0.718	4	0.0046	0.135
5	0.7175	20.989	6	0.0044	0.128
7	0.3562	10.418	8	0.0069	0.202
9	0.0166	0.485	10	0.0031	0.091
11	0.2720	7.955	12	0.0086	0.250
13	0.1499	4.384	14	0.0083	0.244
15	0.0150	0.439	16	0.0041	0.119
17	0.1309	3.830	18	0.0095	0.279
19	0.0741	2.167	20	0.0008	0.024
21	0.0083	0.241	22	0.0011	0.032
23	0.0745	2.180	24	0.0017	0.050
25	0.0329	0.962	26	0.0027	0.080
27	0.0087	0.255	28	0.0012	0.035
29	0.0390	1.142	30	0.0028	0.083
31	0.0158	0.462	32	0.0020	0.060
33	0.0053	0.154	34	0.0008	0.023
35	0.0277	0.810	36	0.0017	0.050
37	0.0111	0.323	38	0.0010	0.031
39	0.0049	0.143	40	0.0005	0.014

PAGE 1/2

Figure 27. FFT result of the source current under unbalanced load, before compensation.

Normal Mode   Uover:■ ■ ■   Scaling:■   LineFilt:■   NULL:■   YOKOGAWA
   Iover:■ ■ ■   Average:■   FreqFilt:■   CF:3

PLL   U1
Freq   50.031 Hz

Urms1   120.22 V
Irms1   4.9011 A
P1   0.5860kW
S1   0.5892kVA
Q1   −0.0615kvar
λ1   0.9945
φ1   D5.99 °

Uthd1   3.337 %
Ithd1   1.649 %
Pthd1   0.005 %

PAGE 1/5

Element1: U1 150V, I1 5A
Element2: U2 150V, I2 5A
Element3: U3 150V, I3 5A
Integ:Reset Time -----:--:--

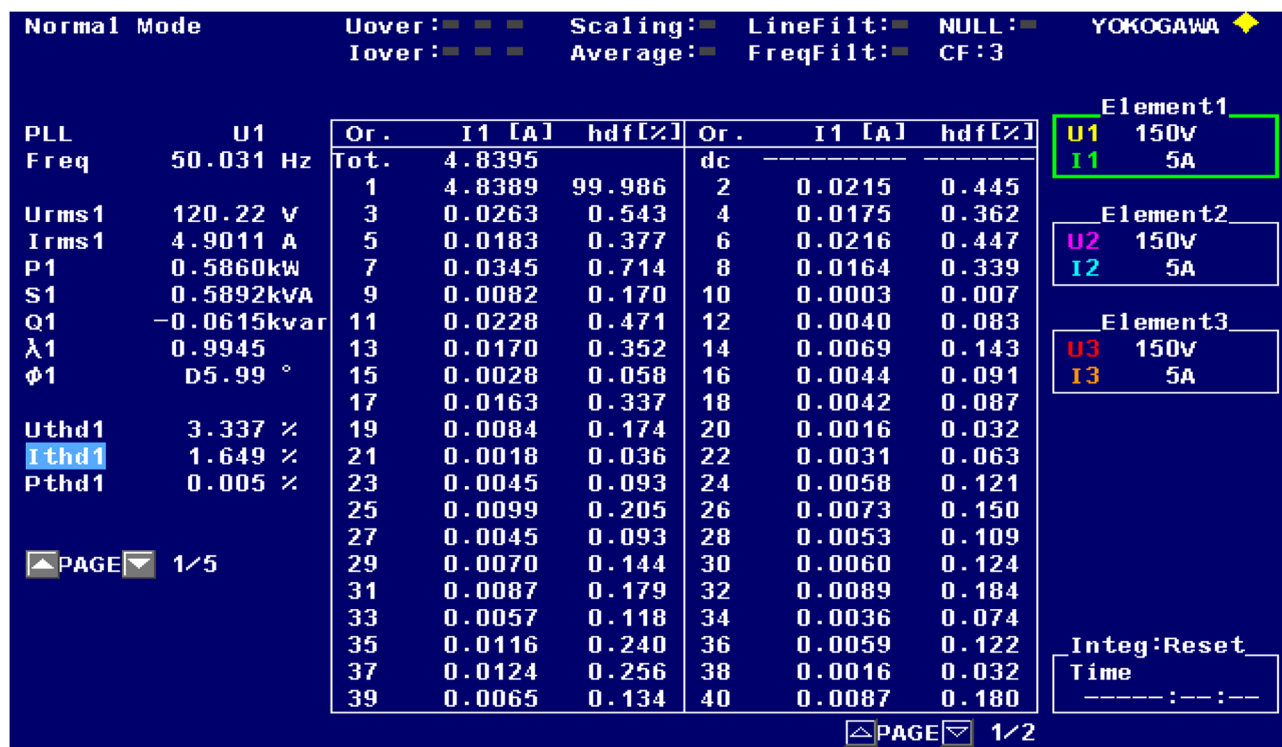| Or.	I1 [A]	hdf[%]	Or.	I1 [A]	hdf[%]
Tot.	4.8395		dc	------	------
1	4.8389	99.986	2	0.0215	0.445
3	0.0263	0.543	4	0.0175	0.362
5	0.0183	0.377	6	0.0216	0.447
7	0.0345	0.714	8	0.0164	0.339
9	0.0082	0.170	10	0.0003	0.007
11	0.0228	0.471	12	0.0040	0.083
13	0.0170	0.352	14	0.0069	0.143
15	0.0028	0.058	16	0.0044	0.091
17	0.0163	0.337	18	0.0042	0.087
19	0.0084	0.174	20	0.0016	0.032
21	0.0018	0.036	22	0.0031	0.063
23	0.0045	0.093	24	0.0058	0.121
25	0.0099	0.205	26	0.0073	0.150
27	0.0045	0.093	28	0.0053	0.109
29	0.0070	0.144	30	0.0060	0.124
31	0.0087	0.179	32	0.0089	0.184
33	0.0057	0.118	34	0.0036	0.074
35	0.0116	0.240	36	0.0059	0.122
37	0.0124	0.256	38	0.0016	0.032
39	0.0065	0.134	40	0.0087	0.180

PAGE 1/2

Figure 28. FFT result of the source current under unbalanced load, before compensation.

Data availability

The datasets used and/or analysed during the current study available from the corresponding author on reasonable request.

References

1. Tandekar, J., Ojha, A. & Jain, S. Real time implementation of multilevel converter based shunt active power filter for harmonic compensation in distribution system. In *2016 7th India International Conference on Power Electronics (IICPE)* 1–5 (2016). https://doi.org/10.1109/IICPE.2016.8079499.
2. Swain, S. D., Ray, P. K. & Mohanty, K. B. Improvement of power quality using a robust hybrid series active power filter. *IEEE Trans. Power Electron.* **32**(5), 3490–3498. https://doi.org/10.1109/TPEL.2016.2586525 (2017).
3. Kumar, R., Bansal, H. O., Gautam, A. R., Mahela, O. P. & Khan, B. Experimental investigations on particle swarm optimization based control algorithm for shunt active power filter to enhance electric power quality. *IEEE Access* **10**, 54878–54890. https://doi.org/10.1109/ACCESS.2022.3176732 (2022).
4. Çelik, D., Ahmed, H. & Meral, M. E. Kalman filter-based super-twisting sliding mode control of shunt active power filter for electric vehicle charging station applications. *IEEE Trans. Power Deliv.* **38**(2), 1097–1107. https://doi.org/10.1109/TPWRD.2022.3206267 (2023).
5. Rao, B. N., Suresh, Y., Panda, A. K., Naik, B. S. & Jammala, V. Development of cascaded multilevel inverter based active power filter with reduced transformers. *CPSS Trans. Power Electron. Appl.* **5**(2), 147–157. https://doi.org/10.24295/CPSSTPEA.2020.00013 (2020).
6. Mishra, A. K. *et al.* PSO-GWO optimized fractional order PID based hybrid shunt active power filter for power quality improvements. *IEEE Access* **8**, 74497–74512. https://doi.org/10.1109/ACCESS.2020.2988611 (2020).
7. Tareen, W. U. K. & Mekhielf, S. Three-phase transformerless shunt active power filter with reduced switch count for harmonic compensation in grid-connected applications. *IEEE Trans. Power Electron.* **33**(6), 4868–4881. https://doi.org/10.1109/TPEL.2017.2728602 (2018).
8. Vodyakho, O. & Mi, C. C. Three-level inverter-based shunt active power filter in three-phase three-wire and four-wire systems. *IEEE Trans. Power Electron.* **24**(5), 1350–1363. https://doi.org/10.1109/TPEL.2009.2016663 (2009).
9. Bai, H., Wang, X., Blaabjerg, F. & Loh, P. C. Harmonic analysis and mitigation of low-frequency switching voltage source inverter with auxiliary VSI. *IEEE J. Emerg. Sel. Top. Power Electron.* **6**(3), 1355–1365. https://doi.org/10.1109/JESTPE.2018.2789982 (2018).
10. Zhang, G. & Yu, J. Open-circuit fault diagnosis for cascaded H-bridge multilevel inverter based on LS-PWM technique. *CPSS Trans. Power Electron. Appl.* **6**(3), 201–208. https://doi.org/10.24295/CPSSTPEA.2021.00018 (2021).
11. Qanbari, T. & Tousi, B. Single-source three-phase multilevel inverter assembled by three-phase two-level inverter and two single-phase cascaded H-bridge inverters. *IEEE Trans. Power Electron.* **36**(5), 5204–5212. https://doi.org/10.1109/TPEL.2020.3029870 (2021).
12. Nguyen, L. V., Tran, H.-D. & Johnson, T. T. Virtual prototyping for distributed control of a fault-tolerant modular multilevel inverter for photovoltaics. *IEEE Trans. Energy Convers.* **29**(4), 841–850. https://doi.org/10.1109/TEC.2014.2362716 (2014).
13. Behera, R. R., Dash, A. R. & Panda, A. K. A novel cascaded transformer coupled multilevel inverter with reduced number of switches for high power applications. *World J. Eng.* **20**, 1025 (2022).
14. Datta, A., Sarker, R. & Hazarika, I. An efficient technique using modified p–q theory for controlling power flow in a single-stage single-phase grid-connected pv system. *IEEE Trans. Ind. Inf.* **15**(8), 4635–4645. https://doi.org/10.1109/TII.2018.2890197 (2019).
15. Mikkili, S. & Panda, A. K. Id-Iq control strategy for mitigation of current harmonics with PI and fuzzy controllers. *Int. Conf. Power Energy Syst.* **2011**, 1–6. https://doi.org/10.1109/ICPES.2011.6156668 (2011).
16. Bajaj, M. *et al.* A lyapunov-function based controller for 3-phase shunt active power filter and performance assessment considering different system scenarios. *IEEE Access* **9**, 66079–66102. https://doi.org/10.1109/ACCESS.2021.3075274 (2021).
17. Bangarraju, J., Rajagopal, V. & Jayalaxmi, A. Reduced DC-link voltage for six-leg DSTATCOM using IcosΦ control algorithm. *Annu. IEEE India Conf. (INDICON)* **2013**, 1–6. https://doi.org/10.1109/INDCON.2013.6725949 (2013).
18. Lin, H. C. Intelligent neural network-based fast power system harmonic detection. *IEEE Trans. Ind. Electron.* **54**(1), 43–52. https://doi.org/10.1109/TIE.2006.888685 (2007).
19. Yu, Z. & Ping, W. Harmonic detection based Hopfield neural network optimum algorithm. In *First International Conference on Innovative Computing, Information and Control—Volume I (ICICIC'06)* 379–382 (2006). https://doi.org/10.1109/ICICIC.2006.290.
20. Srinivasan, D., Ng, W. S. & Liew, A. C. Neural-network-based signature recognition for harmonic source identification. *IEEE Trans. Power Deliv.* **21**(1), 398–405 (2006).
21. Nascimento, C. F. *et al.* Harmonic distortion monitoring for nonlinear loads using neural-network-method. *J. Appl. Soft Comput.* **13**, 475–482 (2013).
22. Hunter, D., Yu, H., Pukish, M. S. III., Kolbusz, J. & Wilamowski, B. M. Selection of proper neural network sizes and architectures—a comparative study. *IEEE Trans. Ind. Inf.* **8**(2), 228–240. https://doi.org/10.1109/TII.2012.2187914 (2012).
23. Arya, S. R & Singh, B. Implementation of kernel incremental metalearning algorithm in distribution static compensator. *IEEE Trans. Power Electron.* **30**(3), 1157–1169. https://doi.org/10.1109/TPEL.2014.2315495 (2015).
24. Arya, S. R & Singh, B. Neural network based conductance estimation control algorithm for shunt compensation. *IEEE Trans. Ind. Inf.* **10**(1), 569–577. https://doi.org/10.1109/TII.2013.2264290 (2014).
25. Dash, A. R., Panda, A. K., Lenka, R. K. & Patel, R. Performance analysis of a multilevel inverter based shunt active filter with RT-EMD control technique under ideal and non-ideal supply voltage conditions. *IET Gener. Transm. Distrib.* **13**(18), 4037–4048 (2019).
26. Dash, A. R., Panda, A. K. & Lenka, R. K. Implementation of EMD-based control algorithm for a cascaded multilevel inverter–based shunt active filter. *Int. Trans. Electr. Energy Syst.* **29**(10), 12087. https://doi.org/10.1002/2050-7038.12087 (2019).
27. Swathi, B. & Tiwari, H. Test automation framework using soft computing techniques. In *2021 International Conference on Advances in Electrical, Computing, Communication and Sustainable Technologies (ICAECT)* 1–4 (2021). https://doi.org/10.1109/ICAECT49130.2021.9392602.
28. Mitra, S. & Hayashi, Y. Neuro-fuzzy rule generation: Survey in soft computing framework. *IEEE Trans. Neural Netw.* **11**(3), 748–768. https://doi.org/10.1109/72.846746 (2000).
29. Pedapenki, K. K., Gupta, S. P. & Pathak, M. K. Application of neural networks in power quality. *Int. Conf. Soft Comput. Tech. Implement. (ICSCTI)* **2015**, 116–119. https://doi.org/10.1109/ICSCTI.2015.7489615 (2015).
30. Behera, R. R., Dash, A. R. & Panda, A. K. Cascaded transformer coupled multilevel inverter based shunt active power filter. *Asian Conf. Innov. Technol. (ASIANCON)* **2021**, 1–6. https://doi.org/10.1109/ASIANCON51346.2021.9544884 (2021).
31. Singh, B. & Kumar, S. Control of DSTATCOM using IcosΦ algorithm. In *2009 35th Annual Conference of IEEE Industrial Electronics* 322–327 (2009). https://doi.org/10.1109/IECON.2009.5414942.

32. Jayaprakash, P., Singh, B. & Kothari, D. P. IcosΦ algorithm based control of zig-zag transformer connected three phase four wire DSTATCOM. In *2012 IEEE International Conference on Power Electronics, Drives and Energy Systems (PEDES)* 1–6 (2012). https://doi.org/10.1109/PEDES.2012.6484299.

33. Thielemans, S., Ruderman, A., Reznikov, B. & Melkebeek, J. Improved natural balancing with modified phase-shifted PWM for single-leg five-level flying-capacitor converters. *IEEE Trans. Power Electron.* **27**(4), 1658–1667. https://doi.org/10.1109/TPEL.2011.2169993 (2012).

34. Cuzmar, R. H., Pereda, J. & Aguilera, R. P. Phase-shifted model predictive control to achieve power balance of CHB converters for large-scale photovoltaic integration. *IEEE Trans. Ind. Electron.* **68**(10), 9619–9629. https://doi.org/10.1109/TIE.2020.3026299 (2021).

35. Iqbal, M. *et al.* Neural networks based shunt hybrid active power filter for harmonic elimination. *IEEE Access* **9**, 69913–69925. https://doi.org/10.1109/ACCESS.2021.3077065 (2021).

36. Hoon, Y., Zainuri, M. A. A. M., Al-Ogaili, A. S., Al-Masri, A. N. & Teh, J. Active power filtering under unbalanced and distorted grid conditions using modular fundamental element detection technique. *IEEE Access* **9**, 107502–107518. https://doi.org/10.1109/ACCESS.2021.3101238 (2021).

Author contributions

Rashmi Rekha Behera: CONCEPT, CONTROL TECHNIQUEAshish Ranjan Dash: RESUT ANALYSISSatyasis Mishra: RESULT ANALYSISAnup Kumar Panda: MethodologyDemissie Jobir Gelmecha: Organization of manuscript

Competing interests

The authors declare no competing interests.

Additional information

Correspondence and requests for materials should be addressed to D.J.G.

Reprints and permissions information is available at www.nature.com/reprints.

Publisher's note Springer Nature remains neutral with regard to jurisdictional claims in published maps and institutional affiliations.